Periodic arrays of deep nanopores made in silicon with reactive ion etching and deep UV lithography

Léon A Woldering[1]**, R Willem Tjerkstra**[1]**, Henri V Jansen**[2]**, Irwan D Setija**[3] **and Willem L Vos**[1,4]

[1] Complex Photonic Systems (COPS), MESA$^+$ Institute for Nanotechnology and Department of Science and Technology, University of Twente, PO Box 217, NL-7500 AE Enschede, The Netherlands

[2] Transducers Science and Technology (TST), MESA$^+$ Institute for Nanotechnology and Department of Electrical Engineering, Mathematics and Computer Science, University of Twente, PO Box 217, NL-7500 AE Enschede, The Netherlands

[3] ASML Netherlands B V, De Run 6501, NL-5504 DR Veldhoven, The Netherlands

[4] FOM Institute for Atomic and Molecular Physics (AMOLF), Kruislaan 407, NL-1098 SJ Amsterdam, The Netherlands

E-mail: l.a.woldering@utwente.nl

Abstract

We report on the fabrication of periodic arrays of deep nanopores with high aspect ratios in crystalline silicon. The radii and pitches of the pores were defined in a chromium mask by means of deep UV scan and step technology. The pores were etched with a reactive ion etching process with SF_6, optimized for the formation of deep nanopores. We have realized structures with pitches between 440 and 750 nm, pore diameters between 310 and 515 nm, and depth to diameter aspect ratios up to 16. To the best of our knowledge, this is the highest aspect ratio ever reported for arrays of nanopores in silicon made with a reactive ion etching process. Our experimental results show that the etching rate of the nanopores is aspect-ratio-dependent, and is mostly influenced by the angular distribution of the etching ions. Furthermore we show both experimentally and theoretically that, for sub-micrometer structures, reducing the sidewall erosion is the best way to maximize the aspect ratio of the pores. Our structures have potential applications in chemical sensors, in the control of liquid wetting of surfaces, and as capacitors in high-frequency electronics. We demonstrate by means of optical reflectivity that our high-quality structures are very well suited as photonic crystals. Since the process studied is compatible with existing CMOS semiconductor fabrication, it allows for the incorporation of the etched arrays in silicon chips.

1. Introduction

The fabrication of spatially periodic nanostructures in silicon receives a great deal of attention in contemporary materials science. Such structures have many interesting applications like photonic crystals [1], chemical sensors [2], as a means to alter the wetting of liquids on a surface [3] and as capacitors in high-frequency electronics [4]. The incorporation of such structures on existing silicon chips is greatly desired, and adapting conventional semiconductor nanofabrication to that end is extensively researched.

A straightforward method to obtain periodic arrays in silicon is the etching of pores in pre-defined patterns and directions. More specifically, to obtain photonic crystals with stop bands in the telecommunication windows (1330 and 1550 nm), the diameter of these pores must be smaller than 500 nm. The pore to pore distances, also referred to as pitch or interpore distance, must be well below 1 μm. Furthermore the depth to diameter aspect ratio of the pores must be as high as possible to obtain photonic crystals with large enough volumes. We would like to obtain pores with

aspect ratios such that the depth of the pores at least exceeds 5 μm. To avoid unwanted scattering of light, the sidewalls must be as smooth as possible [5, 6] and tapering of the pores must be minimized [7]. Finding techniques to make the above-described pores in silicon is extensively researched, see, e.g., [8], and is the focus of this paper.

Several techniques have been developed for the formation of arrays of nanopores in silicon. The electrochemical etching of pores is a beautiful example of a fabrication technique for photonic crystals made by etching [9]. Although structures with impressive aspect ratios have been obtained, this technique is quite complicated and uses non-standard equipment, and is therefore not likely to be incorporated in CMOS semiconductor nanofabrication. Silicon double inversion [10] is another interesting method to realize pores with high aspect ratios. However, this method is rather complex since it requires many preparative steps, including non-CMOS equipment. Since the reported transmittance for wavelengths around 1.5 μm is rather low, the technique seems less suited for making photonic structures with bandgaps in the telecommunication windows.

Since deep reactive ion etching (DRIE), and more specifically the Bosch process [11], is already used in the semiconductor industry, it is interesting to consider this process for etching nanopores. The use of the Bosch process in the semiconductor industry is exemplified by the fabrication of sloping electrodes [12], antireflection structures [13] and high-speed electronics [4]. Recently the Bosch process has also been used to etch high aspect ratio pores with large diameters of 6 μm and interpore distances exceeding 9 μm in silicon [14], and pores with diameters of 1 μm with interpore distances of around 2.3 μm [8]. The two-dimensional photonic crystals formed by these pores have stop bands at wavelengths far exceeding the telecommunication regions. The diameters and pitches of the pores must be reduced to smaller than 1 μm in order to obtain stop bands around 1550 nm. From the literature on one-dimensional trenches with dimensions below 1 μm, we learn that etching such small features is challenging due to effects like aspect-ratio-dependent etching, also known as RIE lag, and that successful etching results require specific processes tuned to the sub-micrometer patterns [15, 16].

An important fabrication aspect is the definition of the required structures by lithography. While e-beam [17] or laser interference lithography [18] are often used in research, deep UV scan and step lithography is the method of choice in semiconductor industry, since it is fast and allows the patterning of large surfaces. Although the incorporation of deep UV lithography into nanophotonic research seems to be in its infancy, interesting results have already been achieved [19, 20].

In this paper we investigate whether we can fabricate nanopores with diameters below 500 nm and pitches well below 1 μm, with high aspect ratios. The nanopores were pre-defined by a chromium mask patterned using deep UV lithography.
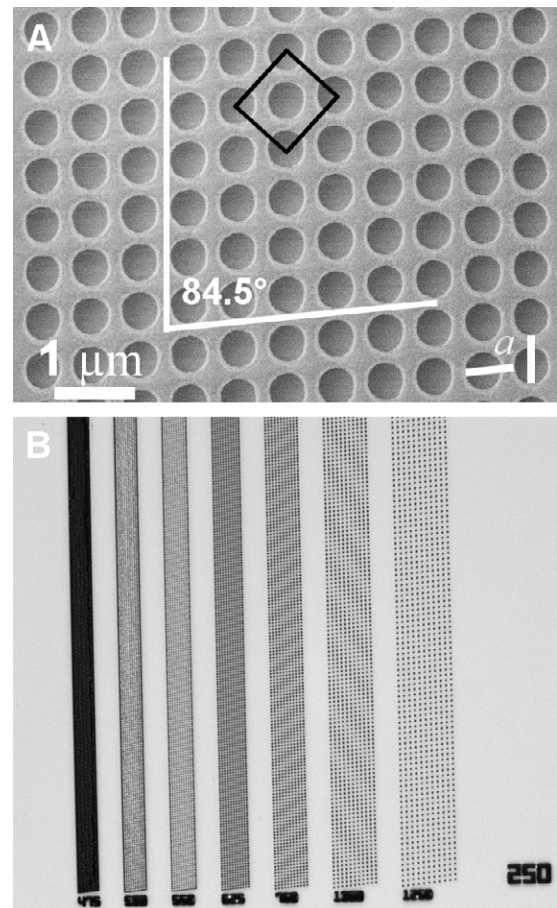
Figure 1. (A) Scanning electron micrograph of the patterned photoresist. The holes in the photoresist are oriented in a centered rectangular lattice, outlined in black. The pitch is the shortest distance between two holes and is indicated by the two short white bars indicated *a*. In this case the pitch *a* equals 600 ± 12 nm and the diameter is $D = 462 \pm 22.5$ nm. The pattern density ϕ is around 47%. Outlined in white are the two axes of the primitive cell, with angle 84.5°. (B) With a concomitant range of pattern densities, the periodic patterns of holes are arranged in different sets of diameter–pitch combinations. In each set the separate lines have the same specified diameter and varying pitches. In the example shown here the specified diameter is $D = 250$ nm, with pitches varying from $a = 475$ to 1250 nm.

2. Experimental details

In this work 200 mm single-crystal silicon wafers were used (p-type, single side polished, (100), 1–10 Ω cm) which were coated with a 50 nm thick chromium layer using electron gun evaporation on a Balzers BAK 600. Subsequently, bottom anti-reflective coating (BARC, DUV 42), photoresist (PEK 445) and topcoat (Aquatar) were spin-coated on the wafers. The resist was patterned using an ASML PAS5500/700 deep UV step and scan system. The pattern was a centered rectangular lattice with a 2 mm type lattice symmetry [21], see figure 1(A), and consisted of many different periodic arrays of holes with a wide range of pitches and a range of hole diameters as shown in figure 1(B). The pitch *a*, or interpore distance, is the shortest distance between two holes and is shown in figure 1(A). This pattern was chosen as it always cleaves through a set of pores

Table 1. Gas flow parameters of the unmodified high aspect ratio structures in silicon recipe. The unit sccm represents a 'standard cubic centimeter per minute'.

|	Gas	Flow (sccm)	Duration (s)
Step 1, protection	C_4F_8	200	1
Step 2, etching	SF_6	250	3

for convenient structural analysis, while it only slightly differs from a square pattern. The angle between the two axes of the primitive cell is 84.5°. The initial pattern density of these structures is the ratio between the etched area and the masked area and is expressed in percentages. After patterning the chromium was etched using chlorine plasma-reactive ion etching. Subsequently the photoresist, BARC and topcoat were removed.

The patterned wafer was cleaved into pieces of approximately 1.5 by 2.5 cm. These pieces were mounted on 100 mm p-type silicon dummy wafers. In order to anchor the sample on the dummy wafer and stabilize its temperature, a small droplet of Fomblin™ vacuum oil was deposited between the sample and the dummy wafer. By applying slight pressure the droplet of oil formed a thin layer between sample and substrate.

The patterned wafers on the dummy wafers were placed in an Adixen Alcatel AMS100SE etcher. The etching parameters we selected are modifications from a Bosch recipe formulated to achieve high aspect ratio structures (HARS) in silicon. The HARS recipe is a two-step process, where in one of the steps the pores are etched and in the other step the pore walls are laminated with a polymer layer. The gas flow parameters of both steps are shown in table 1. In our experiments, the substrate temperature was kept at 10 °C, the capacitively coupled plasma power (CCP) at 80 W (around 260 kHz low frequency, 10 ms on, 90 ms off) and the inductively coupled plasma power (ICP) at 1500 W (13.56 MHz radiofrequency). The distance between the CCP-driven substrate holder and the ICP source was 200 mm. The vacuum throttle valve was completely open.

The two parameters we varied separately in our etching experiments were: (1) the flow of SF_6, which was varied from 31 to 200 sccm to find a flow that yields both a high etching rate and minimal sidewall erosion, and (2) the total etching time, which was chosen between 3 and 12 min in order to study the temporal evolution of the etching process. Furthermore the lithographic mask provides a range of pore diameters and pattern densities.

After etching, the sample was cleaved and the pores near the center of the sample were analyzed using a LEO 1550 high-resolution scanning electron microscope. All pores were imaged from the perpendicular direction (tilt = 0°). Figure 2 shows a schematic outline of an etched pore and its measured dimensions. The measured depth of the pores is indicated as *h*. All reported diameters D_{pore} were measured at half the depth of the pores. Data from up to ten pores were measured and averaged. The error margins of all measurements are determined by the uncertainty in the measurement and the calibration accuracy of the scanning electron microscope,
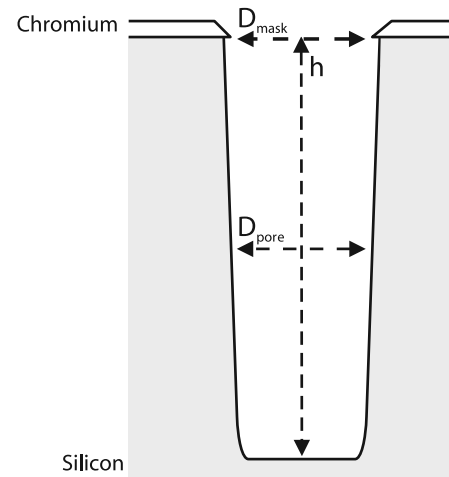
Figure 2. Schematic overview of a pore etched in silicon through a chromium mask. Indicated are both materials, the measured depth of the pores *h*, the measured mask aperture diameter D_{mask} and the measured diameter of the pores D_{pore} at half the pore depth. The sidewall erosion is determined by taking the measured diameter of the etched pores D_{pore}, subtracting the mask aperture diameter D_{mask}, and dividing the result by 2. The aspect ratio *A* is defined as *h* over D_{pore}.

which is accurate within 2%. Similarly, the resist structure and the mask were analyzed by scanning electron microscopy. The measured mask aperture diameter is indicated in figure 2 as D_{mask}. The sidewall erosion was determined by taking the measured diameter of the etched pores D_{pore}, subtracting the mask aperture diameter D_{mask}, and dividing the result by 2. The error margins in the sidewall erosion are given by one-half of the sum of the errors of D_{pore} and D_{mask}. The aspect ratio *A* is defined as *h* over D_{pore}. The total number of samples used in the studies described in this paper was 13, including samples fabricated to test the reproducibility of the process.

Optical reflectivity measurements were performed using illumination from a Fianium supercontinuum white light source. The light beam was focused on the sample with an Ealing 74× reflecting objective with a numerical aperture of 0.65, to a spotsize diameter of around 6 μm. A Biorad FTS-60A spectrometer equipped with a long wavelength InGaAs detector was used to detect the reflected light. References were measured on a gold mirror. For these experiments a sample was used in which the chromium mask was patterned using e-beam lithography with circles in a rectangular pattern which was the (110) plane of a cubic lattice. The diameter of the pores was D_{pore} = 241 ± 16.6 nm and the interpore distance *a* was around 420 nm. The structure was etched in the same way as the others.

3. Results and discussion

3.1. Deep UV lithography

Since the lithography defines the subsequently etched pores, we will briefly analyze the photoresist and chromium mask structures. Figure 1(B) is an optical microscopy image of arrays of holes with one particular specified diameter, and
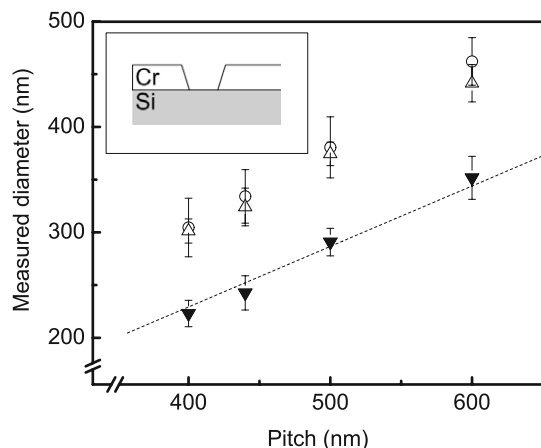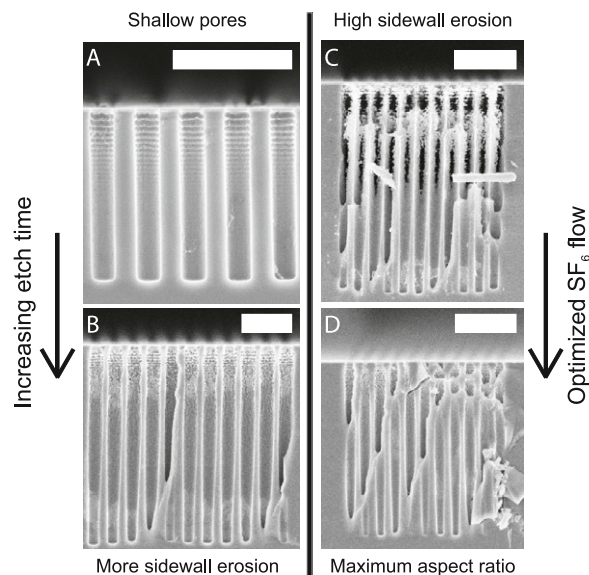
Figure 3. The measured diameter of holes versus the pitch in the mask in the photoresist (circles) and in the chromium layer. As shown schematically in the inset the holes in the chromium layer are tapered. The upward triangles denote the diameter of the holes at the top of the chromium layer. The downward triangles are the hole diameters at the bottom of the chromium layer and are taken as the effective hole diameters. The dotted line is a fit from which the pattern density is found to be $\phi = 25.9 \pm 0.77\%$.

Figure 4. Scanning electron micrograph for a representative set of cleaved samples etched under different conditions. In all images the scale bar equals 2 μm. (A) Pores etched for 3 min with 125 sccm SF_6. The depth of these pores is $h = 2.85 \pm 0.066$ μm and their diameter is $D_{pore} = 421 \pm 17.5$ nm. (B) Pores etched with the same mask for 12 min. These pores have a depth of $h = 7.9 \pm 0.16$ μm. Their diameter is $D_{pore} = 574 \pm 29$ nm. (C) Pores etched for 12 min with 125 sccm of SF_6. The sidewall erosion was significant, causing the pores to break down. (D) Pores etched with the same mask as (C), but with an optimized flow of SF_6 of 62 sccm. These pores have the least sidewall erosion resulting in the highest aspect ratio of 16 ± 1.4, with a pore diameter of $D_{pore} = 351 \pm 21$ nm and a pitch of $a = 484 \pm 9.7$ nm. We estimate the tapering to be about 0.5°.

pitches varying between 475 and 1250 nm. The length of the arrays of holes extends over more than 15 mm, that is more than 15 000 pores. Such large structures are made without stitching, which is an advantage of deep UV lithography over e-beam lithography. Moreover, the simultaneous lithography of different diameter–pitch combinations is an advantage over laser interference lithography.

Figure 1(A) shows a high-resolution scanning electron microscopy image of a photoresist pattern after step and scan processing. The hole diameter is $D = 462$ nm and the pitch is $a = 600$ nm. Data from many such images were analyzed and results are summarized in figure 3 for one particular pattern density. Figure 3 shows the measured hole diameters versus pitch, both for the patterned photoresist and the subsequent chromium mask. The data reveal that the holes in the chromium layer are tapered, as shown schematically in the inset, since the diameters at the top of the layer are systematically larger than at the bottom. The effective mask is defined as the aperture bounded by the bottom of the hole. We thus see that the effective mask aperture diameter is significantly smaller than the diameter defined by the circles in the photoresist pattern. To determine the pattern density of the diameter–pitch combinations shown in figure 3, a line was fitted through the effective mask aperture diameter (downward triangles) and the origin, using linear regression with a confidence of 95%. As shown in appendix A, the slope of this line relates to the pattern density, yielding in this case a value of $\phi = 25.9 \pm 0.77\%$. Since the reactive ion etching of a pattern is influenced by the pattern density [22] it is important to determine this parameter. Furthermore, since the pattern densities of the diameter–pitch combinations shown are equal, these combinations are suitable for further analysis of etching experiments where other processing parameters were varied.

3.2. Nanopores in silicon

Figure 4 gives an overview of how increasing the etching time and reducing the amount of SF_6 influences the etching result. From such scanning electron micrographs the depth and the diameter of the pores were measured. The apparent damage on several structures is due to the cleaving of the sample, but the deeply etched pores are well visible. Figure 4(A) shows a set of pores etched for 3 min with 125 sccm SF_6. These pores have almost no tapering, but with a depth of $h = 2.85$ μm they are not deep enough for our purposes. To fabricate deeper pores we increased the etching time. Figure 4(B) shows pores etched for 12 min with the same mask. These pores are indeed deeper and have a depth of $h = 7.9$ μm. Unfortunately increasing the etching time not only influences the depth of the pores, but also increases sidewall erosion. Therefore the diameter of the pores increases so much that the pores start to break down. The diameter increased from $D_{pore} = 421$ nm after 3 min of etching to $D_{pore} = 574$ nm after 12 min of etching. The tapering of these pores is estimated to be about 0.5°, which is slightly more compared to the 3 min experiment. Figure 4(C) shows another set of pores etched for 12 min with 125 sccm SF_6. In this case the sidewall erosion caused the pores to overlap and break down. To limit the amount of sidewall erosion the amount of SF_6 was reduced. Figure 4(D) shows pores etched with the same mask, but with 62 sccm SF_6. The pores have a diameter of $D_{pore} = 351$ nm and individual pores no longer
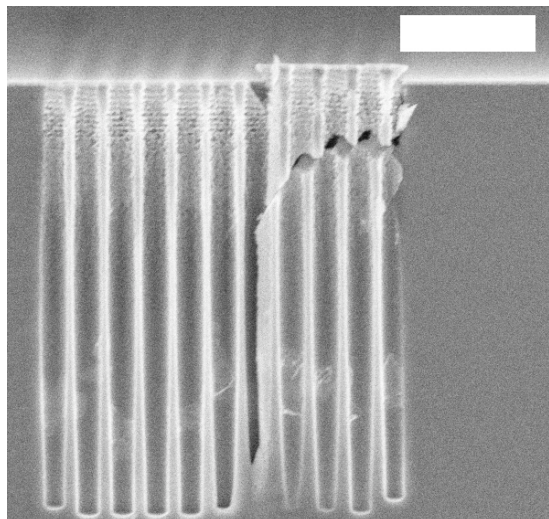
Figure 5. Scanning electron micrograph of deeply etched pores. The surface damage due to cleaving of the sample is limited, allowing excellent visibility of the pores. The interpore distance is $a = 500 \pm 10$ nm, the depth of these pores is $h = 6.4 \pm 0.14$ μm and their diameter is $D_{pore} = 423 \pm 22$ nm, corresponding to an aspect ratio of 15.2 ± 1.1.

overlap, which shows that reducing the flow of SF_6 does yield pores with less sidewall erosion. Although the depth of these pores is slightly less than the pores etched with 125 sccm SF_6, the aspect ratio of these pores is as high as 16. To the best of our knowledge this is the highest aspect ratio ever reported for arrays of nanopores in silicon, etched using a reactive ion etching process. The pores shown in figures 4(B) and (D) have smooth sidewalls, apart from the upper 1–2 μm. The roughness observed in the first micrometers near the surface of the wafer is a sequence of evenly spaced rims caused by the cyclic nature of the Bosch etching process. These rims are commonly referred to as scallop [13, 23]. Figure 5 shows another example of deeply etched pores. In this example, the damage on the cross section due to cleaving of the sample is only limited, and the visibility of individual pores is excellent. The aspect ratio of these pores, which again have smooth sidewalls, is around 15.2. In the next sections we will study in more detail how increasing the etching time and altering the flow of SF_6 influences the depth, diameter and aspect ratio of the obtained pores. We will also study how the observed sidewall erosion was influenced by the flow of SF_6 and the pattern density of the mask.

3.3. Aspect ratio with time

To study any etching process it is important to analyze the evolution of that process as time progresses. The measured diameter, depth and aspect ratio obtained from images similar to figure 4 are plotted as a function of total etching time in figure 6. Data are shown for two different diameter–pitch combinations, with different initial pattern densities ϕ of 5.59 and 11.2%.

In figure 6(A) the pore depths as a function of time are shown. The depth of the pores increases with etching
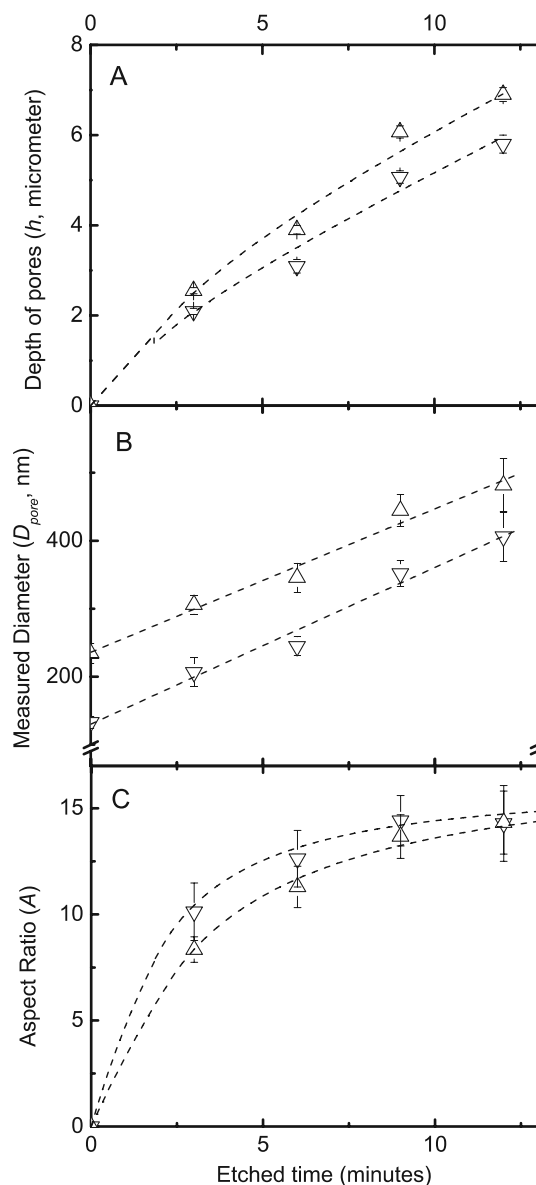
Figure 6. Measured values for two different pattern densities as a function of etching time. The pores were etched with a flow of SF_6 of 125 sccm. The upward triangles indicate a mask aperture diameter of $D_{mask} = 235 \pm 15$ nm and a pitch of $a = 625 \pm 13$ nm, corresponding to a density of $\phi = 11.2 \pm 1.8\%$. The downward triangles indicate a mask aperture diameter of $D_{mask} = 133 \pm 8.6$ nm and a pitch of $a = 500 \pm 10$ nm, corresponding to a density of $\phi = 5.6 \pm 0.94\%$. (A) The measured pore depth versus the etching time. The pore depths increase as etching time progresses, but levels off. The dashed lines show the results for the fits of a model that explains the data (section 3.5, equation (9)). (B) The measured pore diameter as a function of the etching time. The diameter of the pores increases steadily over time. The dashed lines are linear fits. The slope of the fit for pattern density $\phi = 5.59\%$ is 23 ± 1.7 nm min^{-1} and the slope for pattern density $\phi = 11.1\%$ is 21 ± 1.6 nm min^{-1}. (C) The initial aspect ratio rapidly increases, but as the etching progresses the aspect ratio levels off. After $t = 12$ min, the aspect ratio no longer increases. The dashed lines are derived from the same model as in (A), with A equals h over D_{pore}.

time, but the increase levels off slightly as the aspect ratio increases. This means that the etching rate decreases with increasing aspect ratios, which is consistent with an aspect-

ratio-dependent etching process [15]. The dashed lines show the results for the fits of a model to explain the data. We will discuss this in more detail in section 3.5. From figure 6(B) it is apparent that the diameter of the pores steadily increases over time; despite the protection of the sidewall, some sidewall erosion occurs. To determine the rate of sidewall erosion per unit time a straight line was fitted to the data. One-half of the slope of such a line represents the rate of sidewall erosion in nm per minute. The linear relation between measured diameter and etching time shows that the rate of sidewall erosion is constant over time, and not aspect-ratio-dependent. Therefore the aspect ratios that can be achieved with this technique are limited, since the depth increases slower and slower with time, while the diameter increases linearly with time. Figure 6(C) confirms that although initially the aspect ratio increases rapidly, the increase in aspect ratio levels off as etching progresses. At etching times below 12 min we observe that narrower pores have higher aspect ratios, similar to results reported for one-dimensional trenches [12, 24]. At etching times exceeding $t = 12$ min the aspect ratio appears to go towards a maximum. The dashed lines are derived from the same model as in figure 6(A).

3.4. Etching rates and sidewall erosion

3.4.1. Ion angular distribution and image force. In Bosch reactive ion etching the etching rates are usually aspect-ratio-dependent [15]. For sub-micrometer structures with high aspect ratios, two mechanisms have been determined to contribute most significantly. The first mechanism is referred to as the ion angular distribution [15, 25]: due to collisions of ions with gas and the thermal motion of the ions in the plasma glow, ions will travel with an angular distribution towards the pores. Due to this angular distribution of the ions, an increasing fraction of the ions will hit the sidewall of the pores, and less ions are available to etch the bottom of the pores when the pores get deeper. Consequently the average etching rate is reduced as the aspect ratio increases. The ions that hit the sidewalls will cause erosion of the protective layer and therefore increase the amount of sidewall erosion. The second mechanism is commonly referred to as image force or image potential, see, e.g., [15, 25, 26]: a charged particle close to a solid material is attracted due to influencing fields. When a pore or trench is etched, such an image force attracts the incident ions towards the sidewalls and, although the ions may be perfectly collimated, they will be deflected towards the sidewall. As the aspect ratio increases, more ions will hit the sidewall of the pores and less ions will be available to etch the bottom of the pores. The ions that hit the sidewalls will cause erosion of the protective layer and therefore increase the amount of sidewall erosion.

3.4.2. Influence of mask aperture diameter. As a consequence of the aspect ratio dependency of the etching process, we find deeper pores when the mask aperture diameter of the etched pores is larger for equal initial pattern densities. Note that the etching rates at the start of the etching process are assumed to be equal. In order to quantify the dependence on mask aperture diameter, we plotted the etch depth and average etching rate
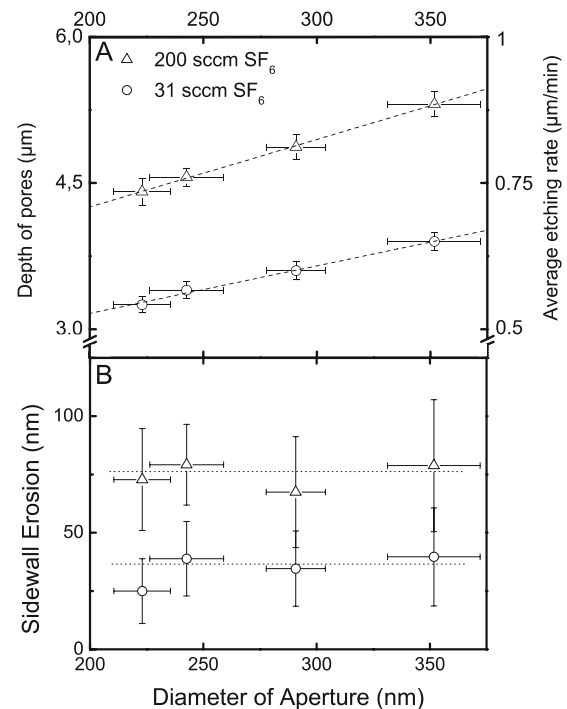

Figure 7. (A) Etch depth (left axis) and average etching rate (right axis) versus mask aperture diameter D_{mask} for etching experiments with 31 and 200 sccm SF_6. The average etching rate was calculated by dividing the measured depth of the pores h by the total etching time (in this case 6 min). The dashed lines are linear fits to the data. The confidence level of the fits was 95% and the coefficients of determination were found to be >0.99. (B) Measured sidewall erosion versus mask aperture diameter D_{mask} for etching experiments with 31 and 200 sccm SF_6. The dotted lines serve as guides to the eye.

versus the mask aperture diameter for the etching experiments with different flows of SF_6, see figure 7(A). The average etching rate was calculated by dividing the measured depth of the pores h by the total etching time (in this case 6 min). The dashed lines are fits to the data and show a linear relation between the average etching rate and the diameter of the holes on the chromium mask. It is expected that the average etching rate will level off at higher mask aperture diameters, analogous to etching results described in the literature [12, 15, 22, 27].

Recent cryogenic reactive ion etching experiments of micrometer-sized one-dimensional trenches in silicon show that the rate of sidewall erosion is equal for differently sized masks [28]. To test if this is also the case for our two-dimensional patterns and our etching process, we have plotted in figure 7(B) the sidewall erosion versus the mask aperture diameter for the experiments with different flows of SF_6. The figure shows that the diameter of the mask aperture does not influence the amount of sidewall erosion. Two of our data points were found to be exceptional, namely the holes with the lowest diameter at flows of 31 and of 62 sccm (not shown in the figure). Pores grown from these displayed even less sidewall erosion. For design purposes it is convenient if sidewall erosion is independent of mask aperture, as it allows a straightforward extrapolation from differently sized patterns to the expected diameter of desired pores.
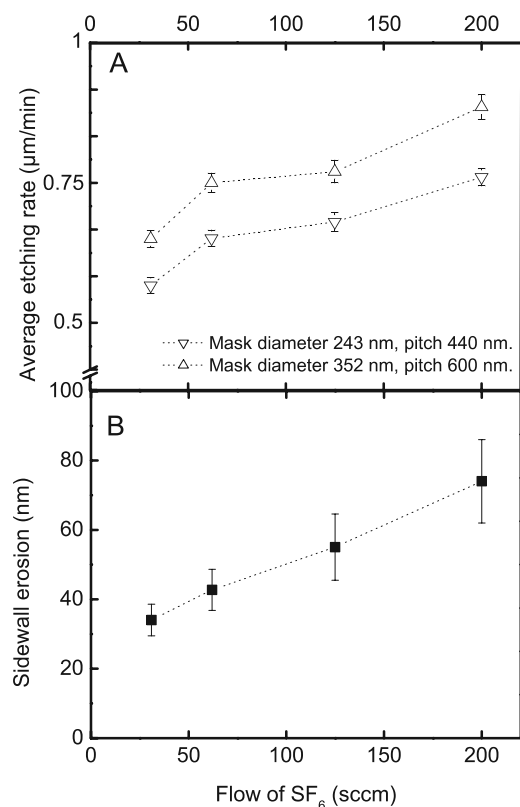
Figure 8. (A) Average etching rate versus the flow of SF$_6$ for two of the diameter–pitch combinations. The dotted lines are guides to the eye. (B) Sidewall erosion of pores after etching for 6 min as a function of the flow of SF$_6$. The sidewall erosion increases with flow.

3.4.3. Influence of etchant flow. To study the effect of the flow of SF$_6$, we measured the diameters and the pore depths of the four diameter–pitch combinations shown in figure 3. The pores were etched for 6 min with different flows of SF$_6$. For two of the diameter–pitch combinations, the average etching rates are shown versus the flow of SF$_6$ in figure 8(A). The figure illustrates that the etching rate is highest at 200 sccm. Pores etched with 125 and 62 sccm SF$_6$ show a reduced etching rate. At 31 sccm the etching rate dramatically decreases and the obtained aspect ratio of the pores is reduced. Obviously, at 0 sccm no etching and sidewall erosion occur.

From the measured diameters we obtained the amount of sidewall erosion, see figure 8(B). For all flows of SF$_6$ sidewall erosion occurred during etching, and at higher flows of SF$_6$ the amount of sidewall erosion is larger. These larger amounts of sidewall erosion are due to the exposure of the sidewalls to the etching plasma being increased, whereas the amount of sidewall protection stays the same. In addition, a higher flow of SF$_6$ results in a higher chamber pressure [29], which causes reduced directionality of the plasma due to collisional scattering of ions [30] and therefore more sidewall erosion. By combining the results for the sidewall erosion and the etching rate, we conclude that an SF$_6$ flow of 62 sccm is optimal, since the amount of sidewall erosion is fairly low while maintaining a sizable etching rate.
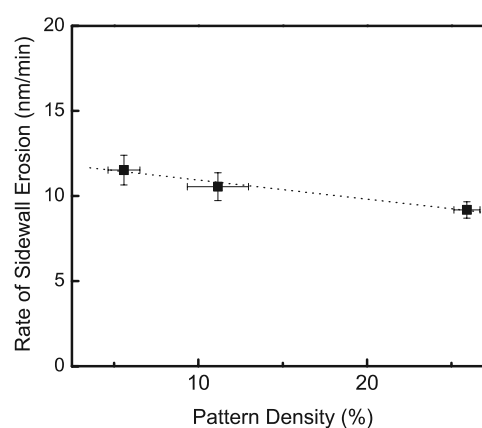
Figure 9. Rate of sidewall erosion as a function of initial pattern density. The dotted line serves as a guide to the eye. At higher pattern densities, the rate of sidewall erosion is reduced. In these experiments the flow of SF$_6$ was 125 sccm.

3.4.4. Pattern density and sidewall erosion. In the previous sections we observed that the rate of sidewall erosion is (a) not aspect-ratio-dependent, and (b) is not influenced by the diameter of the chromium mask. To see whether there is an influence of the pattern density on the rate of sidewall erosion, we plotted in figure 9 the rate of sidewall erosion versus the initial pattern densities of the etched pores. The raw data for the sidewall erosion at $\phi = 5.6$ and 11% are shown in figure 6(B). The results show that, with increasing pattern density, the rate of sidewall erosion slightly decreases. We tentatively explain this result by considering two different possible mechanisms. The first effect is the microloading effect [24, 31], which causes the amount of fluoride radicals to be relatively depleted at higher pattern densities compared to lower pattern densities. Therefore the sidewall erosion, caused by the fluoride radicals diffusing through the polymer protective layer, is reduced at high pattern densities compared to the sidewall erosion at lower pattern densities. The second effect is the sidewall charging [32]: ions colliding with the sidewalls of the etched pores will leave their charge since the sidewalls are covered with an insulating polymer layer. This charge creates an electrostatic field which next repels ions, therefore reducing sidewall erosion. The charge on the sidewall will be compensated with electrons from the silicon behind the polymer layer. At higher initial pattern densities there is less bulk silicon, and therefore less electrons are available to move through the polymer layer. The ion-induced charges will be less rapidly compensated and more ions will be repelled. Consequently the sidewall erosion will be less at higher pattern densities compared to lower pattern densities. Since the initial pattern density is determined by design, it is not possible to use pattern density as a tool to reduce sidewall erosion. Fortunately, however, photonic crystals require structures with a high pattern density where only low rates of sidewall erosion occur.

3.5. Theoretical analysis of time-dependent pore depth

3.5.1. Numerical integrations. To interpret the results of our experiments, we compare our measured pore depths h

versus etching time from figure 6(A) with a theoretical model describing the reactive ion etching process. We apply a model from [25, 33] for one-dimensional trenches to our two-dimensional pore arrays, since we expect the dynamics of the etching to be similar. In the model, the aspect ratio dependence of the etching rate of the process is described by considering the ion angular distribution and the image force effects separately, as well as considering both effects combined. Moreover we would like to investigate whether image force effects are more dominant in our sub-micrometer pores, in contrast to micrometer wide trenches where image force effects can be neglected until very high aspect ratios.

(i) When only the image force effects are considered, the etching rate R as a function of aspect ratio A at etching time t is described by

$$\frac{R(t)}{R_{\max}} = 1 - \left(\frac{kA(t)^2}{E_{\text{kin}}D(t)} \right)^{\left(\frac{1}{3}\right)}. \qquad (1)$$

Here, E_{kin} is the kinetic energy of the ions that is equal to around 40 eV, k is a constant equal to 1×10^{-9} eVm, $D(t)$ is the measured diameter of the pores at time t and $R_{\max}$ is the maximum etching rate.

(ii) In the case where only the ion angular distribution is considered the etching rate $R(t)$ as a function of aspect ratio $A(t)$ is described by

$$\frac{R(t)}{R_{\max}} = \frac{A_{\text{c}}}{A(t)}, \qquad (2)$$

where A_{c} is known as the critical aspect ratio [25]. This equation is valid for $A > A_{\text{c}}$. For $A < A_{\text{c}}$, $R(t) = R_{\max}$.

(iii) The etching rate $R(t)$ as a function of aspect ratio $A(t)$ when considering both the ion angular distribution and the image force effects is described by multiplying equations (2) and (1):

$$\frac{R(t)}{R_{\max}} = \frac{A_{\text{c}}}{A(t)} \left[1 - \left(\frac{kA(t)^2}{E_{\text{kin}}D(t)} \right)^{\left(\frac{1}{3}\right)} \right]. \qquad (3)$$

This equation is valid for $A > A_{\text{c}}$. When $A < A_{\text{c}}$ only the image force effects contribute and equation (1) applies.

We assume that all aspect ratios in figure 6(C) are higher than A_{c}. To calculate the depth of the pores versus etching time, we have integrated equations (1)–(3) numerically. To perform numerical integrations, the above equations had to be rewritten. Firstly $A(t)$ is rewritten as

$$A(t) = \frac{h(t)}{D(t)}, \qquad (4)$$

with $h(t)$ the calculated depth of the pores. $D(t)$ was determined by fitting the measured pore diameter versus etching time with a straight line (see figure 6(B)):

$$D(t) = \alpha t + \beta. \qquad (5)$$

Using equations (4) and (5), equation (1) was rewritten as

$$R(t) = \frac{\text{d}h}{\text{d}t} = \left[1 - \left(\frac{kh(t)^2}{E_{\text{kin}}(\alpha t + \beta)^3} \right)^{\left(\frac{1}{3}\right)} \right] R_{\max}. \qquad (6)$$

Here $R_{\max}$ is taken to be an adjustable parameter. Equation (2) is rewritten as

$$R(t) = \frac{\text{d}h}{\text{d}t} = \frac{(\alpha t + \beta)K}{h(t)}, \qquad (7)$$

where $K = A_{\text{c}}R_{\max}$ is an adjustable parameter. Finally equation (3) is rewritten as

$$R(t) = \frac{\text{d}h}{\text{d}t} = \left[1 - \left(\frac{kh(t)^2}{E_{\text{kin}}(\alpha t + \beta)^3} \right)^{\left(\frac{1}{3}\right)} \right]$$
$$\times \frac{(\alpha t + \beta)K}{h(t)}, \qquad (8)$$

again with K as an adjustable parameter. Numerical integrations were calculated using the Runge–Kutta–Fehlberg fourth–fifth-order procedure in Maple 9. We fitted the numerically integrated equations (6)–(8) to the experimental data for $h(t)$ in figure 6(A) using reduced chi-square minimization. In the procedure the depth of the pores at $t = 3$ min was fixed at their measured values.

(i) When trying to fit with equation (6), where only the image force effects are considered, it was not possible to find a good match between fitted and experimental data within reasonable conditions for $R_{\max}$. Therefore image force effects alone can be excluded as the sole mechanism responsible for the aspect ratio dependence of the etching rates.

(ii) When fitting equation (7), where only the ion angular distribution is considered, the fits yielded values of $K = 5.8$ μm min^{-1} for the upward triangles and of $K = 5.7$ μm min^{-1} for the downward triangles. The χ^2 values were 11.9 and 6.69, respectively. These χ^2 values are elevated, because the reported error bars do not reflect the intrinsic variabilities between separate etching experiments, which could not be quantified. From our experimental data we find that $R_{\max} \geqslant 0.85$ μm min^{-1}. This means that the obtained K values correspond to critical aspect ratios $A_{\text{c}} \leqslant 6.8$ and 6.7, respectively, which is well below the measured aspect ratios at $t = 3$ min. This result validates our initial assumption that all reported aspect ratios in figure 6(C) are higher than A_{c}.

(iii) In the case where both the ion angular distribution and the image force are considered (equation (8)), best fits were found for $K = 7.3$ μm min^{-1} for the upward triangles and for $K = 7.5$ μm min^{-1} for the downward triangles. Our fits yielded χ^2 values of 12.4 and 6.61, respectively. These K values correspond to critical aspect ratios $A_{\text{c}} \leqslant 8.5$ and 8.8, respectively, which is closer to the measured aspect ratios at $t = 3$ min, but still equal to or below that value. Again, this result validates our initial assumption that all reported aspect ratios in figure 6(C) are higher than, or at least equal to, A_{c}.

From the agreement between the fits of equations (7) and (8) and our data, we conclude that, for aspect ratios higher than the critical aspect ratio A_{c}, the ion angular distribution is the most pronounced mechanism that determines the aspect ratio dependence of our etching rates. When considering

both ion angular distribution and image force as the combined mechanisms, we also find reasonable fits, but no improvement. Therefore a contribution of image force effects on the observed etching rates is probably small and can be neglected.

3.5.2. Analytical theory for the ion angular distribution. In the situation that only the ion angular distribution affects the etching process, it is possible to derive an analytical expression for the depth of the pores as a function of etching time. This analytical expression is used to determine R_{max} and A_c of our process. This equation is derived similar as shown in [25] and [33], with the modification that here the sidewall erosion is included:

$$h(t)^2 = \frac{h_c^2}{(\alpha t_c + \beta)t_c}(\alpha t^2 + 2\beta t - \beta t_c), \qquad (9)$$

with t_c the time and h_c the depth of the pores at which A_c is reached. Both are free parameters. This equation is valid for $t \geqslant t_c$. For $t < t_c$, $h(t) = R_{max}t$. When fitting equation (9) to our data we obtain solutions for t_c and h_c. Given that $h_c = A_c(\alpha t_c + \beta)$ and that $h_c = R_{max}t_c$, we can calculate R_{max} and A_c. For the downward triangles we find $R_{max} = 0.73 \pm 0.36$ μm and $A_c = 7.9 \pm 2.1$, with a χ^2 of 6.6. We get the following solution for the upward triangles: $R_{max} = 0.85 \pm 0.21$ μm and $A_c = 6.9 \pm 0.9$, with a χ^2 of 12. These results show that, for an SF$_6$ flow of 125 sccm, A_c is below 8 and that R_{max} is around 0.85 μm, once again validating our initial assumptions. In figure 6(A) we plotted the combined results of the fits of the measured data with equation (9) and the results for the depth of the pores $h(t)$ at etching times below t_c, where $h(t) = R_{max}t$. These plots show that our measured data is indeed well described by an ion angular dependence on the etching rate. In addition, these plots are very useful to determine what etching time is needed to acquire pores with a minimum depth requirement.

　　An advantageous feature of the analytical modeling is that it provides an expression for the maximum aspect ratio A_{max}. While our number of data points is too small to obtain a well-constrained value for A_{max} (17 $\pm$ 10 and 16 $\pm$ 14, for the upward and downward triangles, respectively), equation (10) gives an insight into what mechanism should be improved to further increase the aspect ratio of our pores:

$$A_{max}^2 = \lim_{t \to \infty} A^2 = A_c \frac{R_{max}}{\alpha}. \qquad (10)$$

In this equation we see that increasing both R_{max} and A_c has a beneficial effect on the maximum obtainable aspect ratio A_{max}. Reducing the rate of sidewall erosion $1/2\alpha$ will also improve A_{max}. Reducing the pressure in the system, or increasing the kinetic energy E_{kin} of the ions, will improve the ion angular distribution and therefore increase A_c. However, it is very difficult to obtain A_c values over 10. It is possible to increase R_{max} by, for example, increasing the flow of SF$_6$. Unfortunately, as we have shown, an increase in the flow of SF$_6$ results in more sidewall erosion and both effects counteract. The best and most promising option to increase the maximum obtainable aspect ratio A_{max} is to reduce α, equal to two
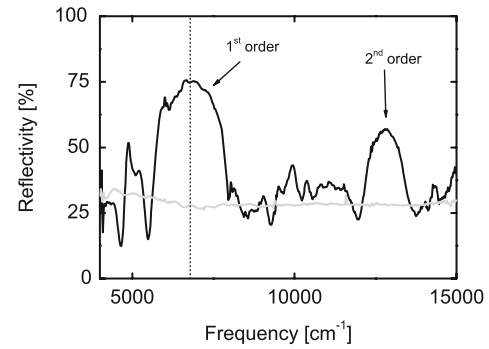
Figure 10. Optical reflectivity measurement of a two-dimensional photonic crystal. Shown is the measured reflectivity versus frequency. The arrows indicate the first-and second-order stop bands around 6800 cm^{-1} and 12 800 cm^{-1}, respectively. The dotted line shows the estimated value for the first-order stop band calculated using Bragg's law. The gray line is a background measurement on bulk silicon.

times the rate of sidewall erosion, to values close to zero. For example, better sidewall protection can be achieved by enhancing the protecting step of the Bosch process. Fine-tuning of the C$_4$F$_8$ step by increasing the step time or the flow of C$_4$F$_8$ can decrease sidewall erosion to very low values at unmodified etching steps and unchanged A_c, increasing the maximum aspect ratio of our pores significantly.

3.6. Optical reflectivity

Optical reflectivity measurements were performed on a two-dimensional photonic structure fabricated using our modified Bosch reactive ion etching process. Figure 10 shows the measured reflectivity versus frequency. Visible are two major peaks centered around $k = 6800$ cm^{-1} and 12 800 cm^{-1}, which show excellent reflectivity of our crystal as high as 75%, much higher than the 30% reflectivity of bulk silicon.

　　Using the geometric details of the pores, and Bragg's law [34] adapted to photonic crystals [35], the central frequency of the first-order stop band can be calculated as

$$\lambda(\text{nm}) = \frac{10^7}{k(\text{cm}^{-1})} 2n_{eff} \frac{a(\text{nm})}{\frac{1}{2}\sqrt{3}} \qquad (11)$$

with λ the first-order Bragg reflection in nm, n_{eff} the effective refractive index and a the interpore distance. The effective refractive index n_{eff} is calculated from the dielectric constants of air ε_{air}, of silicon ε_{Si} and the pattern density ϕ:

$$n_{eff} = \sqrt{\left(\frac{\phi}{100}\varepsilon_{air}\right) + \left(\left(1 - \frac{\phi}{100}\right)\varepsilon_{Si}\right)}. \qquad (12)$$

We take $\varepsilon_{air} = 1$ and $\varepsilon_{Si} = 12.25$. The dotted line shown in figure 10 is the calculated first-order Bragg reflection for the sample. From the excellent agreement with the center of the peak, the first peak is identified as the first-order stop band and the second peak as the second. A more detailed assignment of the reflectivity features is currently underway. The width of the first-order stop band is around 30%, which suggest that

the photonic strength of our sample is high. These results show that our two-dimensional structures are well suited for optical experiments, and also that our fabrication process is compatible with optical experiments and applications.

4. Conclusions

We have presented a 'Bosch-type' reactive ion etching method to fabricate deep nanopores with high aspect ratios of more than 16 in monocrystalline silicon. We etched pores with diameters smaller than 500 nm and pitches smaller than 1 μm, which have low tapering and smooth sidewalls. In order to etch these high aspect ratio pores, the sidewall erosion was minimized, while maintaining a high etch rate. We have shown that the sidewall erosion is not influenced by the diameter of the holes in the mask. Furthermore, the rate of sidewall erosion is not aspect-ratio-dependent, and constant over time. Masks with smaller holes yield pores with higher aspect ratios, analogous to results in the literature describing the etching of one-dimensional trenches.

Since the sidewall erosion is reduced with decreasing flows of SF$_6$, a low SF$_6$ flow must be balanced against the etching rate. We concluded that etching with an SF$_6$ flow near 62 sccm was optimal to achieve high aspect ratio pores. We have also shown that the sidewall erosion decreases with increasing pattern density, which is favorable for photonic crystal applications.

By evaluating experiments with different flows of SF$_6$ and with different pattern densities, we have determined that our etching process is aspect-ratio-dependent. Firstly, our time-dependence study shows that the etching rate decreases when the time etched, and thus the aspect ratio, increases. Secondly, our data of the etch rate as a function of aspect ratio agree well with an existing model for aspect-ratio-dependent reactive ion etching. At aspect ratios higher than A_c the ion angular distribution appears to contribute most significantly to the aspect ratio dependence of the etching process. A contribution of image force effects is probably small and can be neglected. We calculated the critical aspect ratio A_c and the initial etching rate R_{max} of our process with a flow of 125 sccm SF$_6$. Furthermore, we show that reducing the amount of sidewall erosion is the most powerful tool to improve the maximum obtainable depth of the pores. Less sidewall erosion is realized by applying more sidewall protection by, for example, increasing the C$_4$F$_8$ flow and/or the time of the protection step of the Bosch process.

Our modified Bosch reactive ion etching process is very suitable for the etching of arrays of high aspect ratio nanopores in monocrystalline silicon. To the best of our knowledge the pores have the highest aspect ratio reported to date for arrays of nanopores in silicon, made with a reactive ion etching process. This enables the fabrication of photonic crystals with large volumes, which also opens an avenue towards the fabrication of three-dimensional crystal structures. We also show that reducing the sidewall erosion is the best way to maximize the aspect ratio of our sub-micrometer structures. Increasing the etching rate has a far less significant effect. Furthermore, we successfully performed optical reflectivity measurements on such a two-dimensional sample and observed intense reflectivity peaks. Our measurement shows that the expected and measured reflectivity peaks are in good agreement. Therefore we conclude that our CMOS-compatible fabrication process is compatible with nanophotonic applications.

Acknowledgments

Appendix

For a two-dimensional array of pores, the pattern density ϕ is defined as

$$\phi = \frac{S_{hole}}{S_{unitcell}}100\%, \tag{13}$$

with S_{hole} the surface of one hole in the mask and $S_{unitcell}$ the surface of the primitive unit cell of the lattice. Using a centered rectangular lattice, equation (13) can be rewritten to contain a linear relation between the square of the diameter and of the pitch:

$$\phi = \frac{\frac{1}{4}\pi D^2}{a^2 \sin(\varphi)}100\%, \tag{14}$$

with φ the lattice angle, in our case $\varphi = 84.5°$.

Therefore, the relation between the diameter D and the pitch of the holes a for a constant pattern density is linear:

$$D = ba, \tag{15}$$

with b the slope of the line.

Equations (15) and (14) combined yield an expression for the pattern density in terms of the experimentally determined slope:

$$\phi = \frac{\frac{1}{4}\pi b^2}{\sin(\varphi)}100\%. \tag{16}$$

References

[1] Yablonovitch E 1987 *Phys. Rev. Lett.* **58** 2059–62
[2] Lee Y J and Braun P V 2003 *Adv. Mater.* **15** 563–6
[3] Martines E, Seunarine K, Morgan H, Gadegaard N, Wilkinson C D W and Riehle M O 2005 *Nano Lett.* **5** 2097–103
[4] Roozeboom F *et al* 2006 *Thin Solid Films* **504** 391–6
[5] Bogaerts W, Bienstman P and Baets R 2003 *Opt. Lett.* **28** 689–91

[6] Gerace D and Andreani L C 2005 *Photon. Nanostruct.* **3** 120–8

[7] Ferrini R, Houdré R, Benisty H, Qiu M and Moosburger J 2003 *J. Opt. Soc. Am.* B **20** 469–77

[8] Chelnokov A, David S, Wang K, Marty F and Lourtioz J M 2002 *IEEE J. Sel. Top. Quantum Electron.* **8** 919–27

[9] Matthias S, Müller F, Jamois C, Wehrspohn R B and Gösele U 2004 *Adv. Mater.* **16** 2166–70

[10] Tétreault N, von Freymann G, Deubel M, Hermatschweiler M, Pérez-Willard F, John S, Wegener M and Ozin G A 2006 *Adv. Mater.* **18** 457–60

[11] Laermer F and Schilp A 1996 *US Patent* 5501893

[12] Rao M P, Aimi M F and MacDonald N C 2004 *Appl. Phys. Lett.* **85** 6281–3

[13] Chang C, Wang Y F, Kanamori Y, Shi J J, Kawai Y, Lee C K, Wu K C and Esashi M 2005 *J. Micromech. Microeng.* **15** 580–5

[14] Zhou M, Chen X, Zeng Y, Xu J and Lu W 2004 *Solid State Commun.* **132** 503–6

[15] Gottscho R A, Jurgensen C W and Vitkavage D J 1992 *J. Vac. Sci. Technol.* B **10** 2133–47

[16] Marty F, Rousseau L, Saadany B, Mercier B, Français O and Mita Yand Bourouina T 2005 *Microelectron. J.* **36** 673–7

[17] Broers A N, Hoole A C F and Ryan J M 1996 *Microelectron. Eng.* **32** 131–42

[18] Prodan L, Euser T G, van Wolferen H A G M, Bostan C, de Ridder R M, Beigang R, Boller K J and Kuipers L 2004 *Nanotechnology* **15** 639–42

[19] Bogaerts W, Baets R, Dumon P, Wiaux V, Beckx S, Taillaert D, Luyssaert B, van Campenhout J, Bienstman P and van Thourhout D 2005 *J. Lightwave Technol.* **23** 401–12

[20] Märki I, Salt M, Herzig H P, Stanley R, Melhaoui L E, Lyan P and Fedeli J 2005 *J. Appl. Phys.* **98** 013103

[21] Kittel C 1967 *Introduction to Solid State Physics* (London: Wiley)

[22] Kiihamäki J, Kattelus H, Karttunen J and Franssila S 2000 *Sensors Actuators* **82** 234–8

[23] Villanueva G, Plaza J A, Sánchez-Amorez A, Bausells J, Martínes E, Samitier J and Errachid A 2006 *Mater. Sci. Eng.* C **26** 164–8

[24] Yeom J, Wu Y, Selby J C and Shannon M A 2005 *J. Vac. Sci. Technol.* B **23** 2319–29

[25] Jansen H V, de Boer M, Wiegerink R, Tas N, Smulders E, Neagu C and Elwenspoek M 1997 *Microelectron. Eng.* **35** 45–50

[26] Davis R J 1991 *Appl. Phys. Lett.* **59** 1717–9

[27] Chou Z K A and Najafi K 2002 *Proc. 15th IEEE Int. Conf. on MEMS (Las Vegas, NV, Jan.)* pp 145–8

[28] Boufnichel M, Lefaucheux P, Aachboun S, Dussart R and Ranson P 2005 *Microelectron. Eng.* **77** 327–36

[29] de Boer M J, Gardeniers J G E, Jansen H V, Smulders E, Gilde M J, Roelofs G, Sasserath J N and Elwenspoek M 2002 *J. Microelectromech. Syst.* **11** 385–401

[30] Jurgensen C W 1988 *J. Appl. Phys.* **64** 590–7

[31] Rangelow I W 2003 *J. Vac. Sci. Technol.* A **21** 1550–62

[32] Jansen H V, de Boer M and Elwenspoek M 1996 *Proc. IEEE, The 9th Ann. Int. Workshop Micro Elec. Mech. Syst.* pp 250–7

[33] Elwenspoek M and Jansen H V 1998 *Silicon Micromachining* (Cambridge: Cambridge University Press)

[34] Bragg W L 1913 *Proc. Camb. Phil. Soc.* **17** 43–57

[35] Vos W L, Sprik R, Blaaderen A V, Imhof A, Lagendijk A and Wegdam G H 1996 *Phys. Rev.* B **53** 16231–5